

# LuMaMi28: Real-Time Millimeter-Wave Massive MIMO Systems with Antenna Selection

MinKeun Chung, *Member, IEEE*, Liang Liu, *Member, IEEE*, Andreas Johansson, Sara Gunnarsson, *Student Member, IEEE*, Martin Nilsson, Zhinong Ying, *Fellow, IEEE*, Olof Zander, Kamal Samanta *Senior Member, IEEE*, Chris Clifton, Toshiyuki Koimori, Shinya Morita, Satoshi Taniguchi, Fredrik Tufvesson, *Fellow, IEEE*, and Ove Edfors, *Senior Member, IEEE*

**Abstract**—This paper presents LuMaMi28, a real-time 28 GHz massive multiple-input multiple-output (MIMO) testbed. In this testbed, the base station has 16 transceiver chains with a fully-digital beamforming architecture (with different pre-coding algorithms) and simultaneously supports multiple user equipments (UEs) with spatial multiplexing. The UEs are equipped with a beam-switchable antenna array for real-time antenna selection where the one with the highest channel magnitude, out of four pre-defined beams, is selected. For the beam-switchable antenna array, we consider two kinds of UE antennas, with different beam-width and different peak-gain. Based on this testbed, we provide measurement results for millimeter-wave (mmWave) massive MIMO performance in different real-life scenarios with static and mobile UEs. We explore the potential benefit of the mmWave massive MIMO systems with antenna selection based on measured channel data, and discuss the performance results through real-time measurements.

**Index Terms**—Antenna selection, beam steering, beamforming, massive multiple-input multiple-out (MIMO), millimeter-wave (mmWave), real-time testbed.

## I. INTRODUCTION

Millimeter-wave (mmWave) communications, operating in the 30 GHz-300 GHz, provide a promising approach. Since large bandwidths can be exploited, it achieves very high peak and cell-edge rates [1], [2]. However, there are fundamental differences between mmWave and traditional sub-6 GHz communication systems. For example, propagation characteristics and hardware constraints. As it is widely known, mmWave signals suffer from high free-space path loss (FSPL), which is inversely proportional to the wavelength  $\lambda$  [3]. The insertion losses and intrinsic power-overhead of mmWave integrated circuits (ICs) result in diminishing gains [4]. Furthermore, the mmWave system is more sensitive to hardware impairments, such as phase noise, power amplifier (PA) nonlinearities [5], [6], [7]. It gives rise to technical challenges in the design and implementation of mmWave systems. To address the challenges,

we present LuMaMi28, a real-time mmWave massive multiple-input multiple-out (MIMO) systems that both analog- and digital-domain architectures are integrated.

### A. Related Work

Over the past few years, the indoor/outdoor mmWave channels have been extensively studied from propagation measurements [8], [9], [10]. To overcome the high FSPL and establish the links with sufficient signal-to-noise ratio (SNR), a large-scale antenna system, so-called massive MIMO, should be needed for beamforming gain [11]. A smaller wavelength allows to use more antennas in the same physical space, resulting in higher array gains, as compared to the system with a larger wavelength. The massive MIMO approach in mmWave frequencies, however, is still prohibitive due to the high hardware cost and power consumptions [12], [13]. As a feasible solution to the problems, a hybrid beamforming architecture has been considered, which has a much lower number of transceiver (TRx) chains than the total antenna number. The number of TRx chains is only lower-limited by the number of data streams transmitted, while the beamforming gain is given by the number of antenna elements if suitable radio frequency (RF)/analog beamforming is done [14]. Motivated by this fact, various hybrid beamforming architectures have been proposed in different papers [15], [16], [17], [18], [19], to achieves near-optimal performance with lower cost and power consumption. Furthermore, finding an appropriate RF/analog beamforming solution has been an active research area in recent years. [20], [21], [22] have presented mmWave antennas, and [23], [24], [25] designed front-end modules, to support RF/analog beamforming. With the RF/analog beamforming strategies, mmWave-specific baseband processing algorithms, such as channel estimation [26], [27] and precoder [12], [16], [28], have been studied for cost- and energy-efficient systems.

A full implementation of mmWave massive MIMO systems, which includes RF/analog- and digital-domain solutions, is an essential work for its practical use, but another significant challenge. Both industry and academia have been making efforts in building mmWave massive MIMO testbed. Samsung [29] and Qualcomm [30] have presented 28 GHz massive MIMO prototypes, and provided their measurements and experimental results. Yang *et al.* [31] and Kuai *et al.* [32] have presented a 64-TRx fully-digital beamforming-based testbed, operating at 28 GHz and 37 – 42.5 GHz band, respectively. Recently, our research team has demonstrated the initial version of LuMaMi28 at IEEE Wireless Communication and Networking Conference

M. Chung, L. Liu, A. Johansson, S. Gunnarsson, M. Nilsson, F. Tufvesson, and O. Edfors are with the Department of Electrical and Information Technology, Lund University, Lund, 221 00, Sweden (e-mail: {firstname.lastname}@eit.lth.se).

Z. Ying and O. Zander are with Sony Research Center Lund, Sweden (e-mail: {firstname.lastname}@sony.com).

K. Samanta and C. Clifton are with Sony Semiconductor and Electronic Solutions, Hampshire, UK (e-mail: {firstname.lastname}@sony.com).

T. Koimori, S. Morita, S. Taniguchi are with Sony Semiconductor Solutions, Analog LSI Business Division, Atsugi, Kanagawa, Japan (e-mail: {firstname.lastname}@sony.com).

This work is carried out within the Strategic Innovation Program “Smartare Elektroniksystem”, a joint venture of Vinnova, Formas and the Swedish Energy Agency (2018-01534).

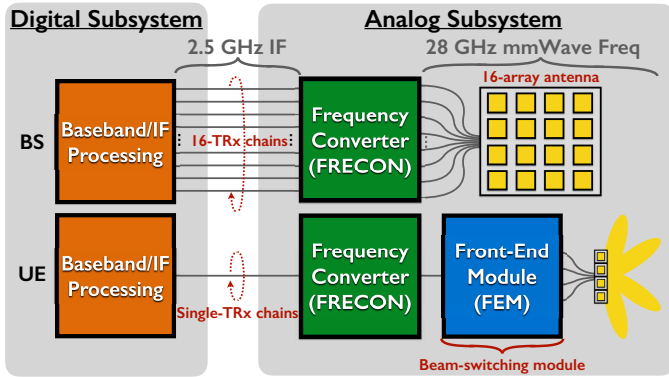


Fig. 1. System overview of our proposed mmWave massive MIMO testbed. A BS and an UE, respectively, consists of analog and digital subsystems.

in 2020 [33], and presented a 28 GHz hybrid beamforming testbed with a 64-antenna/16-TRx unit [34]. However, to the best knowledge of the authors, none of the existing work on mmWave massive MIMO testbeds considers an user equipment (UE)-side beam-steering approach.

### B. Contributions

We develop LuMaMi28, a real-time 28 GHz massive MIMO testbed, simultaneously supporting multiple UEs. Fig.1 illustrates a high-level overview of LuMaMi28 BS and UE. The BS has 16 TRx chains with a fully-digital beamforming architecture. The UEs are equipped with a beam-switchable antenna array for antenna selection. To investigate the impact of different UE antennas, we adopt yagi and patch UE antennas, which have different beam-width and different peak-gain. Our main contributions are summarized as follows:

- LuMaMi28 provides a flexible mmWave massive MIMO system for testing everything from baseband processing algorithms to scheduling and antenna selection in real-propagation environments. We extended the capability of an existing 100-antenna/100-TRx massive MIMO testbed [35], operating below 6 GHz, to build LuMaMi28 BS. The digital subsystem contains different equalizers /precoders, and the analog subsystem is designed in a modular way, for expanding to larger array sizes.
- LuMaMi28 UE has a real-time beam-steering capability for antenna selection. The paper presents a co-design of analog/digital subsystems and its implementation, for this functionality. The proposed algorithm in the digital domain is designed on the field-programmable gate array (FPGA) embedded in the software-defined radio (SDR), and the analog modules are developed in-house.
- We explore potential benefits achieved by the proposed antenna selection algorithm. To better assess the potential gains, a real-channel capture experiment was conducted, where the captured data is uplink (UL) channels between LuMaMi28 BS and UE.
- This paper presents real-time measurement results of LuMaMi28 in static and mobility environments. It studies the system performance with antenna selection, according to different digital-beamforming algorithms and different UE antennas.

### C. Notation

The set of complex numbers is denoted by  $\mathbb{C}$ . Lowercase boldface letters stand for column vectors and uppercase boldface letters designate matrices. For a vector or a matrix, we denote its transpose, conjugate, and conjugate transpose  $(\cdot)^T$ ,  $(\cdot)^*$ , and  $(\cdot)^H$ , respectively; The  $N \times N$  identity matrix is denoted by  $\mathbf{I}_N$ . Sets are designated by upper-case calligraphic letter. A zero-mean circularly-symmetric complex-valued Gaussian random variable  $x$ , with variance  $\sigma^2$ , is denoted as  $x \sim \mathcal{CN}(0, \sigma^2)$ .

### D. Outline of the Paper

In the remainder of the paper is organized as follows. In Section II, we overview the architecture of LuMaMi28. Section III and Section IV describe the design and implementation of digital and analog subsystem, respectively, in LuMaMi28. In Section V, we provide real-time measurement results of LuMaMi28, in different static and mobility scenarios. A summary and concluding remarks appear in Section VI.

## II. LUMAMI28 OVERVIEW

This section provides an overview of LuMaMi28 architecture. LuMaMi28 consists of analog and digital subsystems, as shown in Fig.1. We employ the physical hardware setup of below-6 GHz massive MIMO testbed [35] to construct the digital subsystem including 16-TRx chains. The analog subsystem developed in-house, is combined for supporting mmWave bands. While the BS has the fully-digital beamforming architecture, the UEs adopt a hybrid beamforming architecture for antenna selection, i.e., higher number of antennas than that of TRx chain. Before delving into details, we refer the reader to Table I, which includes high-level system parameters of LuMaMi28.

TABLE I  
HIGH-LEVEL SYSTEM PARAMETERS OF LUMAMI28

Parameter	Value
Carrier frequency	27.95 GHz
Intermediate frequency	2.45 GHz
Sampling frequency	30.72 MHz
Signal bandwidth	20 MHz
FFT size	2048
Antenna-array configuration	16 elements (BS) / 4 elements (UE)
Number of TRx chains	16 (BS) / 1 (UE)
Number of maximum UEs	12
Power gain of FRECON	9 dB (Tx) / 7 dB (Rx)
Power gain of FEM	14 dB (Tx) / 12 dB (Rx)
Peak gain of a BS antenna	5 dBi
Peak gain of UE1 / UE2 antennas	7.5 dBi (yagi) / 10.0 dBi (patch)
Power gain of each Tx chain	22 dB (linear region)
P1dB of each Tx chain	18 dBm
Frame time	10 ms
Beam sweeping duration	10 ms (40 ms for four RF ports)
Guard time for beam switching	71.9 $\mu$ s

The digital subsystem is in charge of baseband and intermediate frequency (IF) processing. A central control unit has an embedded controller (NI PXIe-8135) or a laptop, for the BS and UE, respectively, which runs *LabVIEW* on a standard Windows 7 64-bit operating system to configure and control LuMaMi28.

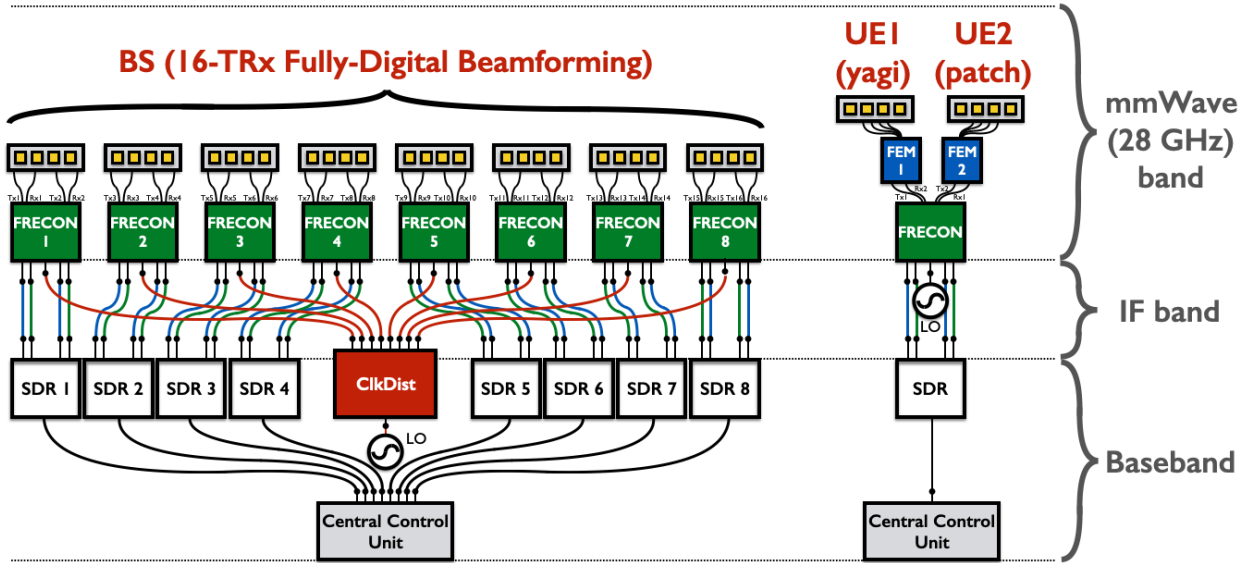


Fig. 2. Architectures of LuMaMi28 BS (16-TRx fully-digital beamforming) and UEs (antenna selection by using a 4-antenna/1-TRx unit). This setup was used for measurement campaigns that we will present in Section V. DC control signals from each SDR, i.e., for TDD and beam switching, are delivered to FRECON (only TDD switching signal) and FEM (both). For simplicity, the routes for the DC control signals are omitted in this figure.

LabVIEW provides both host and FPGA programming. The central control unit for the BS and UE, respectively, is plugged into eight and one SDRs (NI USRP-294xR/295xR). Each SDR is equipped with two TRx chains and a Kintex-7 FPGA. The SDR performs local processing on a per-TRx basis, e.g., orthogonal frequency division multiplexing (OFDM) processing and reciprocity calibration. In the central control unit of the BS, co-processing FPGA modules (FlexRIO 7976R) is included for digital-beamforming processing. To be able to synchronize 16 TRx chains, a reference clock source (PXIe-6674T) and reference clock distribution network (Octo-Clock) are used.

The BS and UE analog subsystems contain in common identical frequency converters (FRECONs) and a common local oscillators (LOs), respectively, for up/down conversion between IF and 28 GHz bands. The BS has a clock distribution module (ClkDist) for amplifying and distributing the LO signal to multiple FRECONs, and each UE has a front-end module (FEM) for beam steering. For reconfigurability and scalability of LuMaMi28, we designed the FRECON and FEM printed circuit boards (PCBs) in a modular way. Each module is equipped with a small number of TRx chains, i.e., two per FRECON and one per FEM. A basic configuration is that, therefore, one FRECON is plugged with one SDR, which can construct two TRx chains for the BS, and two UEs with single TRx chain. Both FRECON and FEM have SPDT switches for time-division duplex (TDD) operation while the FEM has additionally a SP4T switch for switching analog-domain beams. The FRECON contains up/down conversion mixers, low pass filters (LPFs), driver amplifiers (DAs), and low-noise amplifiers (LNAs); the FEM a PA, an LNA, and an LPF for achieving better output power and noise-floor performance. Eight FRECONs in the BS plugs into a 16-element array antenna, and FEM in each UE into a 4-element array antenna. As mentioned earlier, yagi and patch antennas are used to explore the impact of different UE antennas on system performances.

To control the analog subsystem, i.e., for TDD switching and antenna selection, we adopt wired links between analog and

digital subsystems. DC control signals (3.3V) are operated by an implemented control unit in the digital subsystem. We use a 15-pin general-purpose input/output (GPIO) port in each SDR to deliver the control signals. Fig.2 illustrates the architecture of LuMaMi28 BS and UE that we used for measurements.

### III. DIGITAL SUBSYSTEM DESIGN AND IMPLEMENTATION

In this section, the digital subsystem details in LuMaMi28 are discussed based on the aforementioned testbed architecture. To build the digital subsystem, we need to make a few design decisions. First, we reused in part the frame structure and baseband functionalities, such as OFDM, time/frequency synchronization and precoders/equalizers, of the below-6 GHz massive MIMO testbed [35]. Second, a LuMaMi28 UE has the beam-switching capability in the analog subsystem. To operate this, we design an antenna selection algorithm and implement the proposed algorithm in the digital subsystem. Third, notice that control signals for TDD and beam-switching need to be sent from the digital to the analog subsystem. Hence an analog-subsystem control unit has to be implemented in the digital subsystem. In the following subsection, we describe key precoders and equalizers built in the digital subsystem of LuMaMi28.

#### A. Baseband Precoding and Equalization

We consider a simplified model of a multi-user (MU)-MIMO system. The system includes one BS equipped with  $M$  TRx-chains simultaneously serving  $K$  single TRx-chain UE in TDD operation. To reduce the channel-estimation overhead, we adopt a fully digital reciprocity-based beamforming. Based on the fact that an UL propagation-channel matrix  $\mathbf{H}_p \in \mathbb{C}^{M \times K}$  is reciprocal, the estimated UL channel can be exploited to compute precoding matrices for downlink (DL) transmission. The  $K$  UEs transmit their UL data  $\mathbf{s}_{ul} \in \mathbb{C}^K$  in the same time-frequency resource. The average UL power levels used by the  $K$  UEs during transmission are represented by  $\mathbf{p}_{ul} =$

$[p_1, p_2, \dots, p_K]^T$ . The received signals  $\mathbf{y}_{\text{bs}} \in \mathbb{C}^{M \times 1}$  at the BS is

$$\mathbf{y}_{\text{bs}} = \mathbf{H}_{\text{ul}} \sqrt{\mathbf{P}_{\text{ul}}} \mathbf{s}_{\text{ul}} + \mathbf{z}_{\text{bs}}, \quad (1)$$

where  $\mathbf{H}_{\text{ul}} \in \mathbb{C}^{M \times K}$  is the UL channel<sup>1</sup>  $\mathbf{P}_{\text{ul}} \in \mathbb{C}^{K \times K}$  the diagonal matrix with the entries of  $\mathbf{p}_{\text{ul}}$  on its main diagonal,  $\mathbf{z}_{\text{bs}} \in \mathbb{C}^{K \times 1}$  the additive white Gaussian noise (AWGN) with i.i.d.  $\mathcal{CN}(0, 1)$  entries. The detected UL symbols  $\hat{\mathbf{s}}_{\text{ul}} \in \mathbb{C}^{K \times 1}$  by using an equalization matrix  $\mathbf{F}_{\text{eq}} \in \mathbb{C}^{K \times M}$  is

$$\hat{\mathbf{s}}_{\text{ul}} = \mathbf{F}_{\text{eq}} \mathbf{y}_{\text{bs}}. \quad (2)$$

The received signal vector at the UEs in the DL  $\mathbf{y}_{\text{dl}} \in \mathbb{C}^{K \times 1}$  is

$$\mathbf{y}_{\text{ue}} = \mathbf{H}_{\text{dl}} \mathbf{F}_{\text{pr}} \mathbf{s}_{\text{dl}} + \mathbf{z}_{\text{ue}}, \quad (3)$$

where  $\mathbf{H}_{\text{dl}} \in \mathbb{C}^{K \times M}$  is the DL channel,  $\mathbf{F}_{\text{pr}} \in \mathbb{C}^{M \times K}$  the precoding matrix at BS,  $\mathbf{s}_{\text{dl}} \in \mathbb{C}^{K \times 1}$  the DL data vector intended for the  $K$  UEs,  $\mathbf{z}_{\text{ue}} \in \mathbb{C}^{K \times 1}$  the AWGN with i.i.d.  $\mathcal{CN}(0, 1)$  entries. Note that the UL and DL channels are generally not reciprocal in practical systems due to differences of analog circuitry in UL and DL channels as follows.

$$\mathbf{H}_{\text{ul}} = \mathbf{R}_{\text{bs}} \mathbf{H}_{\text{p}} \mathbf{T}_{\text{ue}}, \quad (4)$$

$$\mathbf{H}_{\text{dl}} = \mathbf{R}_{\text{ue}} \mathbf{H}_{\text{p}}^T \mathbf{T}_{\text{bs}}. \quad (5)$$

where the diagonal matrices  $\mathbf{R}_{\text{bs}} \in \mathbb{C}^{M \times M}$  and  $\mathbf{R}_{\text{ue}} \in \mathbb{C}^{K \times K}$  model the non-reciprocal hardware responses of BS and UE receivers, respectively; the diagonal matrices  $\mathbf{T}_{\text{bs}} \in \mathbb{C}^{M \times M}$  and  $\mathbf{T}_{\text{ue}} \in \mathbb{C}^{K \times K}$  hardware responses of BS and UE transmitters, respectively. From (4) and (5), the precoding matrix includes a calibration matrix  $\mathbf{C} \triangleq \mathbf{T}_{\text{bs}} \mathbf{R}_{\text{bs}}^{-1}$  [36]. For the digital subsystem, we consider three linear equalizers/precoders, maximum ratio combining (MRC)/maximum ratio transmission (MRT), zero-forcing (ZF), and regularized ZF (RZF), i.e.,

$$\mathbf{F}_{\text{eq}} = \begin{cases} \mathbf{H}_{\text{ul}}^H & \text{for MRC} \\ (\mathbf{H}_{\text{ul}}^H \mathbf{H}_{\text{ul}})^{-1} \mathbf{H}_{\text{ul}}^H & \text{for ZF} \\ (\mathbf{H}_{\text{ul}}^H \mathbf{H}_{\text{ul}} + \alpha_{\text{eq}} \mathbf{I}_K)^{-1} \mathbf{H}_{\text{ul}}^H & \text{for RZF} \end{cases}, \quad (6)$$

$$\mathbf{F}_{\text{pr}} = \begin{cases} \mathbf{C} \mathbf{H}_{\text{ul}}^* & \text{for MRT} \\ \mathbf{C} \mathbf{H}_{\text{ul}}^* (\mathbf{H}_{\text{ul}}^H \mathbf{H}_{\text{ul}})^{-T} & \text{for ZF} \\ \mathbf{C} \mathbf{H}_{\text{ul}}^* (\mathbf{H}_{\text{ul}}^H \mathbf{H}_{\text{ul}} + \alpha_{\text{pr}} \mathbf{I}_K)^{-T} & \text{for RZF} \end{cases}, \quad (7)$$

where  $\alpha_{\text{eq}}$  and  $\alpha_{\text{pr}}$ , respectively, is a regularization constant that allows trade-off between array gain and interference suppression. The optimal trade-off of  $\alpha_{\text{eq}}$  and  $\alpha_{\text{pr}}$  results in minimum mean-square error (MSE) precoder/equalizer [37].

<sup>1</sup> $\mathbf{H}_{\text{ul}}$  represents the UL radio channel including both the propagation channel  $\mathbf{H}_{\text{p}}$  and the UL hardware transfer functions. Its factorization is shown in (4).

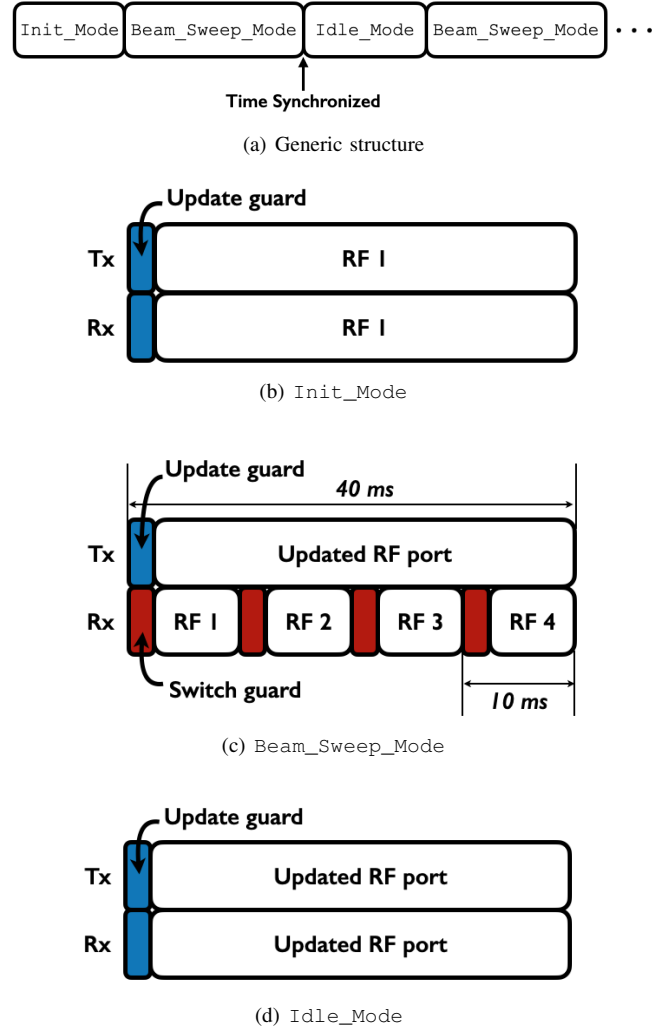


Fig. 3. Antenna selection mode. Each mode has an update guard (blue) or a switch guard time (red) for beam sweeping or updating.

### B. Antenna Selection Algorithm

The basic idea for antenna selection is as follows. Each UE performs a regular beam sweeping in the reception mode. The DL channel estimation block calculates the channel magnitude for each beam. Based on the calculation, the UE selects the one with highest channel magnitude. For real-time operation, the antenna selection algorithm should ensure that the beam sweeping and its channel-magnitude calculation can be synchronized, further, a selected beam can be updated on time. This subsection describes an architecture of the antenna selection algorithm.

The proposed algorithm is designed on the FPGA embedded in the SDR and integrated with baseband functionalities of each UE. For its implementation, we define three modes regarding antenna selection process, as illustrated in Fig. 3. All modes include an update guard or a switch guard time for beam updating and sweeping, respectively. Both the guard time slots have one OFDM symbol duration (71.9  $\mu\text{s}$ ). First, *Init\_Mode* is to set up an initial RF port. We employ the first RF port (RF1) as the initial port for both transmit (Tx) and Rx. As mentioned in Section II, the FEM is switchable among four RF ports. *Beam\_Sweep\_Mode* is to switch among the four receive (Rx) ports where each RF port is switched



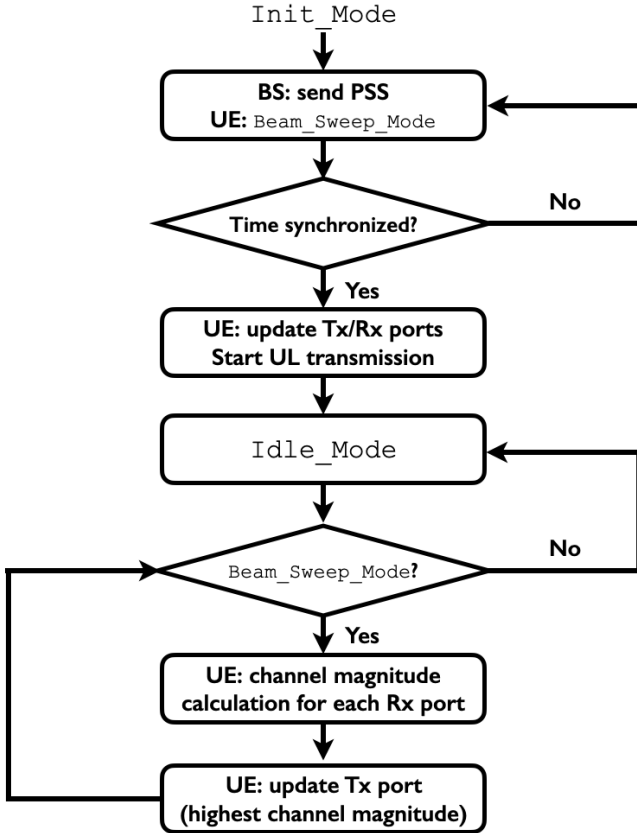


Fig. 4. Flow chart for our antenna selection implementation.

every 10 ms (one frame<sup>2</sup>) in order. Notice that there are two different targets in the use of *Beam\_Sweep\_Mode*. One is for aligning beams before timing synchronization. The other is for calculating DL channel magnitudes for each beam, after timing synchronization. A narrow beam direction at both a mmWave BS and UEs results in low SNR before beamforming, i.e., in isotropic propagation conditions [38]. Hence, a beam alignment through *Beam\_Sweep\_Mode* is required for timing synchronization. In this *Beam\_Sweep\_Mode*, without channel-magnitude calculation, the index of RF port used for a successful time synchronization is updated for both Tx and Rx mode. It is the difference with the other *Beam\_Sweep\_Mode*. During *Beam\_Sweep\_Mode*, the RF port for transmission is determined by the result of previous beam switching, and its updated beam is kept (in case of *Beam\_Sweep\_Mode* before time synchronization, initial RF port, i.e., RF1). Lastly, *Idle\_Mode* does not include switching operation and its period is adjustable unlike *Beam\_Sweep\_Mode* (40 ms). Using an updated beam from the previous mode, the RF port for both transmission and reception is fixed during *Idle\_Mode*.

Fig.4 abstracts the architecture of the antenna selection algorithm. For over-the-air (OTA) synchronization of BS and UEs, we exploit the LTE primary synchronization signal (PSS) generated from a frequency-domain Zadoff-chu sequence [39]. After *Init\_Mode*, the LuMaMi28 BS broadcasts the PSS, and UEs enter *Beam\_Sweep\_Mode* for the beam alignment.

<sup>2</sup>As mentioned earlier, we reused the frame structure of the existing below-6 GHz massive testbed [35], which is long-term evolution (LTE) like TDD-based frame structure. We adopt one frame duration to synchronize beam-sweeping operation and its channel-magnitude calculation in an effective way.

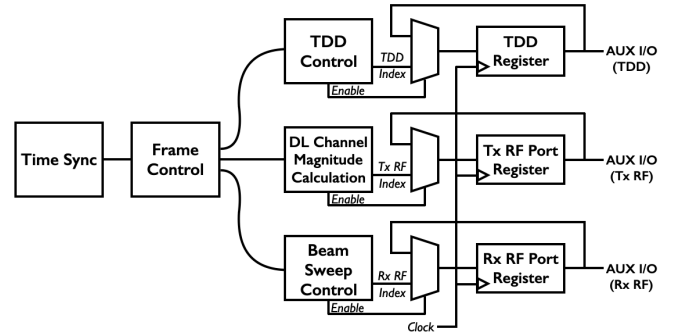


Fig. 5. Block diagram of analog-subsystem control unit. Since an 1-bit index for the TDD switching, and a 2-bit index for RF Tx and Rx, respectively, for the antenna selection, are needed, the same number of registers (five in total) are required to control the analog subsystem. It is simplified in this figure.

If the start of the frame is estimated by the OTA time synchronization, each UE starts the UL transmission, and operates in *Idle\_Mode* until before the next *Beam\_Sweep\_Mode* for calculating DL channel magnitudes. The beam updated for this *Idle\_Mode* is formed by the RF port that makes a success of time synchronization. We design the *Beam\_Sweep\_Mode*, operated after being time-synchronized, so that the switch of RF port, its channel-magnitude calculation, and the antenna-index update of the higher channel magnitude can be accommodated within one frame. Furthermore, all the above operations are synchronized by using a sample counter, resulting in preventing a mismatch between the operations. For example, incorrect mapping between a switched beam and its channel-magnitude calculation, and delayed update of selected beam.

### C. Analog-Subsystem Control Unit

There is two control signals to be delivered from the digital to the analog subsystem. One is an 1-bit TDD index, and the other a 2-bit RF-index for the antenna selection. We also implemented an analog-subsystem control unit on the FPGA embedded in the SDR. Fig.5 illustrates a simplified block diagram of the implemented analog-subsystem control unit. The frame control unit includes the master sample-counter mentioned in the previous subsection, and play a role in synchronizing the following three units. In the DL channel magnitude calculation and beam sweep control units, there is a slave counter, respectively, for *Beam\_Sweep\_Mode*. Each index is written to the dedicated register with 2-to-1 multiplexer, followed by an AUX I/O connection.

Both FRECON and FEM have an interface, respectively, which are connected with the GPIO port. The interface in FRECON is for receiving only TDD control signal, and the one in FEM for both TDD switching and antenna selection. Since the GPIO port plugs in to AUX I/O ports of an FPGA embedded in each SDR, the DC signal (3.3 V) is controllable according to the implemented analog-subsystem control unit in the digital subsystem. To formulate the delay of control signal from digital to analog subsystem, the following four delays introduced from hardware units needs to be considered: 1) delay on rising (falling) edge in the digital subsystem ( $\Delta_d$ ), 2) SPDT switching delay of FRECON ( $\Delta_{sd}^{fre}$ ), 3) SPDT switching delay of FEM ( $\Delta_{sd}^{fem}$ ), and 4) SP4T switching delay of FEM ( $\Delta_{s4}^{fem}$ ).

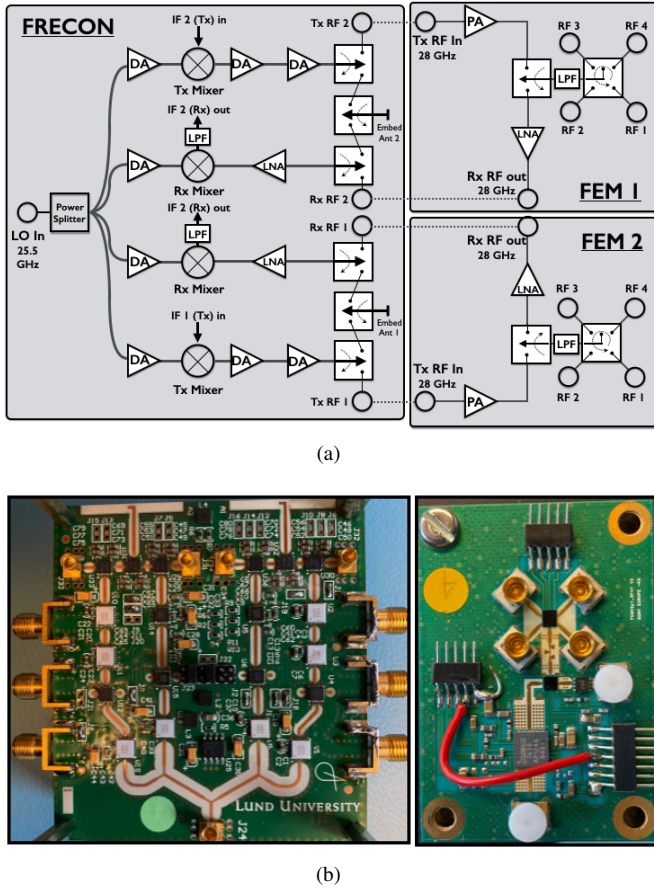


Fig. 6. FRECON and FEM: (a) block diagram with one FRECON and two FEMs in an UE (b) photographs of fabricated FRECON (left) and FEM (right).

The total delay from digital subsystem to FRECON and FEM, respectively, is

$$\Delta_{\text{frecon}} = \Delta_d + \Delta_{\text{sd}}^{\text{fre}}, \quad (8)$$

$$\Delta_{\text{fem}} = \Delta_d + \Delta_{\text{sd}}^{\text{fem}} + \Delta_{\text{s4}}^{\text{fem}}. \quad (9)$$

Based on the measurement, each delay results in  $\Delta_d \simeq 100$  ns,  $\Delta_{\text{sd}}^{\text{fre}} \simeq 20$  ns,  $\Delta_{\text{sd}}^{\text{fem}} \simeq 85$  ns, and  $\Delta_{\text{s4}}^{\text{fem}} \simeq 200$  ns, respectively. It is shown that the guard time ( $71.9 \mu\text{s}$ ) is enough for TDD switching and antenna selection ( $\Delta_{\text{frecon}} \simeq 120$  ns and  $\Delta_{\text{fem}} \simeq 385$  ns).

#### IV. ANALOG SUBSYSTEM DESIGN AND IMPLEMENTATION

RF-interference suppression is crucial to achieve a sufficient output power of each TRx chain. Also, beam switchability is one of key design features in the analog subsystem, to operate the proposed antenna selection algorithm in the digital subsystem. This section elaborates on the design of FRECON, FEM, ClkDist, and UE antenna arrays. Furthermore, its implementation details are discussed.

##### A. FRECON and FEM

MmWave systems are more sensitive to PA nonlinearities, compared to conventional systems below-6 GHz. For the FRECON design, we focused on an appropriate architecture

design and component selection to reduce the PA nonlinearities. As mentioned in Section II, one FRECON has two TRx chains, and connects with four elements of 16-element array antenna in the BS, with two FEMs in the UE. A combined block diagram of FRECON and FEM in an UE is shown in Fig. 6(a). The FRECON contains the same eight DAs (HMC383LC4) but has different targets. Four DAs between an LO-input port and mixers is for amplifying the 25.5 GHz-LO signal, and the other four DAs for the 28 GHz Tx signal. The mixers (HMC1063LP3E) are used for up/down-conversion between IF and 28 GHz bands, where an LO power of more than 10 dBm is required to operate it. That is the reason why a DA for amplifying the LO signal is needed for each mixer. The conversion gain of the mixer is around  $-10$  dB. To compensate this power loss and achieve high output power, the Tx chain is equipped with two consecutive DAs. On the other hand, each Rx chain contains an LNA (HMC1040LP3CE) to avoid compression. In the front-end of the FRECON, there are SPDT switches (ADRF5020) for TDD switching<sup>3</sup>. A 2.45 GHz-band LPF (SAFEA2G45) is included between Rx mixer and IF port.

The employment of FEM is to support testing of long-range communications, as well as beam-switching. As depicted in Fig. 6(a), one FEM contains an additional PA (MAAP-011246) and LNA, which have a high power gain. The SP4T switch engages with four RF ports, and performs switching or selecting by control signals from digital subsystem. For the TDD /beam-switching, the isolation between paths in the switches is important. Both SPDT and SP4T switches were designed in-house using Sony's SOI process. They achieve a low insertion loss of 1.5 dB and 1.6 dB, respectively, and a high isolation of 30 dB and 26 dB, respectively, at 28 GHz. For suppressing the second harmonic in Tx mode, and the high-frequency out-of-band spurious, including from 60 GHz (WLAN/WiFi), in Rx mode operation, an LPF was incorporated between SPDT and SP4T. The insertion loss of this filter plays a very critical role for achieving better output power and noise-floor performance the module. A novel LPF was designed on PCB using distributed elements where capacitors were realized from radial stubs. This approach could realize the filter within a very compact size. It attains a very low insertion/return loss of less than 0.7 dB and  $-18$  dB, respectively, at 28 GHz, and the harmonic rejection of more than 30 dBc.

Based on the measurements of each module [34], the Tx and Rx gains for the FRECON are around 9 dB and 7 dB, respectively. For the FEM, around 14 dB and 12 dB, respectively, is achieved. The Tx gain in its linear region is around 22 dB. It delivers a 1-dB gain compression point (P1dB) of 18 dBm. The maximum Rx gain is 18.8 dB at 27.95 GHz. Also, the power consumption of the implemented FRECON and FEM is 6.3 W and 7 W, respectively. Photographs of the fabricated FRECON and FEM are shown in Fig. 6(b).

##### B. ClkDist

The block diagram of the ClkDist and its photograph are shown in Fig. 7. The ClkDist has 1 input and 8 output ports connecting with the LO (PLDRO-25500-10) and FRECONs,

<sup>3</sup>We integrated two commercial antennas for future work, together with four RF ports. Thus, there are a total of six SPDT switches to control all the RF inputs/outputs of FRECON.

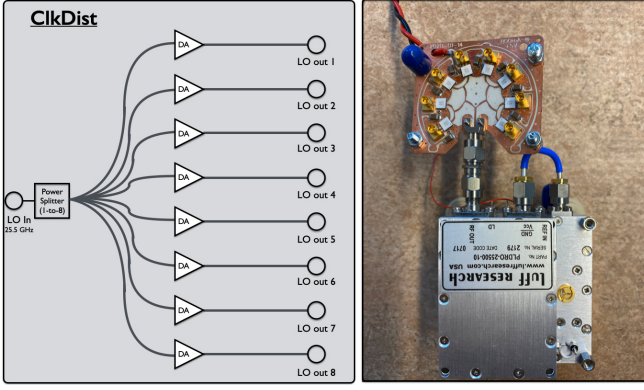


Fig. 7. Block diagram of ClkDist (left) and its photograph with a common 25.5 GHz-LO (right).

respectively. Since the 1-to-8 power splitter causes a power loss of more than 10 dB, each path in the ClkDist is equipped with one DA (HMC383LC4) to meet the input-power requirement of mixers in FRECON. The power consumption of the fabricated ClkDist and the LO is 4 W and 5 W, respectively<sup>4</sup>.

### C. Antenna Array

We designed two UE array antennas for evaluating system performances. Fig. 8 shows photographs and beam patterns of two array antennas. Fig. 8(a) is a wideband (26 GHz to 40 GHz) Yagi antenna [40] with multiple beam points to different directions, which forms a wide angle coverage. It is designed on a two-layer PCB using RO3003 substrate. Four elements were used for beam selection, where each antenna gain is, respectively, 7.5 dBi, 7.0 dBi, 7.0 dBi, and 7.5 dBi. Fig. 8(b) show a  $2 \times 2$  patch antennas with a butler matrix, capable of forming four directional beams. It is designed on a three-layer PCB using two stacked RO4350B substrates. The antenna-element spacing in the subarray is half a wavelength ( $\lambda/2$ ), i.e., 5.5 mm. The peak antenna gain and its bandwidth are around 10 dBi and 1.5 GHz. Both antennas have linear polarization.

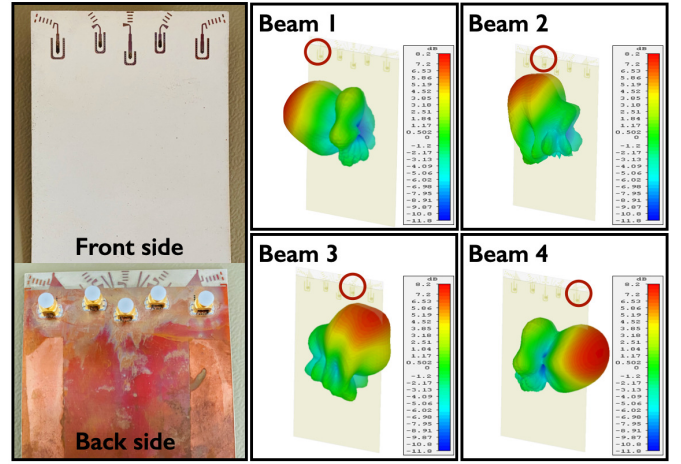
## V. MEASUREMENT RESULTS

This section uses measurement results from static and mobility environments to study the system performance of LuMaMi28. The main measurement campaigns are as follows. First, a path loss measurement with yagi and patch antennas was carried out, where the measured path losses are compared to theoretical ones. Second, a real-channel data between LuMaMi BS and UEs was captured to explore potential gains, achieved by the proposed antenna-selection algorithm. Lastly, real-time performance of LuMaMi28 in a variety of mobility environments was measured. According different digital-beamforming algorithms and different UE antennas, the LuMaMi28 performance results will be presented. In the next subsection, we will describe our measurement scenarios followed by the performance details.

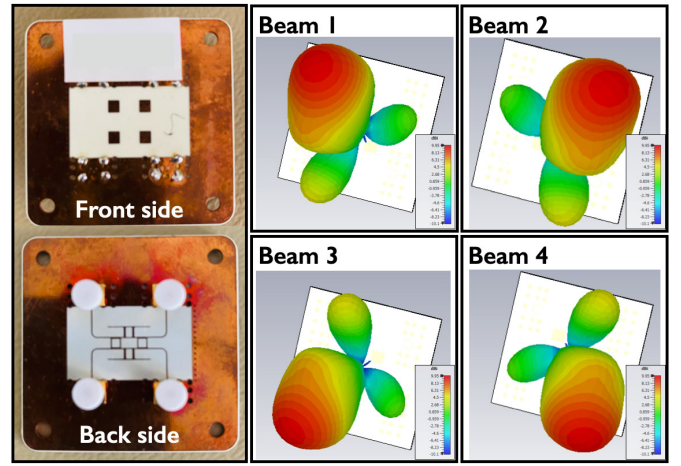
### A. Measurement Scenarios

1) *LuMaMi28 Setup*: A LuMaMi28 BS and two UEs were used, where the BS and each UE have 16-TRx chains and a

<sup>4</sup>LOs operating at mmWave frequencies is very sensitive to temperatures. Thus, we adopt a cooling fan to operate our 25.5 GHz-LO. Its power consumption is added in the LO's power consumption.



(a) yagi antenna



(b) patch antenna

Fig. 8. Photograph and beam pattern of UE antenna arrays. Four elements (out of five) of yagi antenna were used for beam selection. The peak gain of yagi antenna are 7.5 dBi, 7.0 dBi, 7.0 dBi, and 7.5 dBi, respectively, in the antenna-port order. The peak gain of patch antenna has around 10 dBi in each antenna port.

4-antenna/single-TRx unit, respectively, as shown in Fig. 2. All the measurement campaigns were performed in E-huset building at Lund University. Fig. 9 shows photos and indoor maps of our measurement campaign. We selected a long corridor and a large lecture hall for the static and mobility experiments, respectively. In the corridor, the distance between the BS and UEs ranged from 3 m to 11 m, as depicted in Fig. 9(a). Here, a path loss measurement, an UL channel data recording, and an UE rotation test were performed. We will provide more details on measurement results in the long corridor in Section V-B – Section V-D. In the lecture hall, we performed mobility tests with three different routes, as shown in Fig. 9(b). The BS looked at the whiteboard at a fixed spot. Based on the BS location, the green line is for the circled route, the blue for the vertical route, and the red for the horizontal route. Two UEs were co-located on a moving cart. This cart moved with a pedestrian speed of around 3 km/h in each route. The transmit power of both UEs is fixed over all the measurement scenarios. Fig. 10 shows a captured UL Tx power spectrum at a FEM Tx port. We will



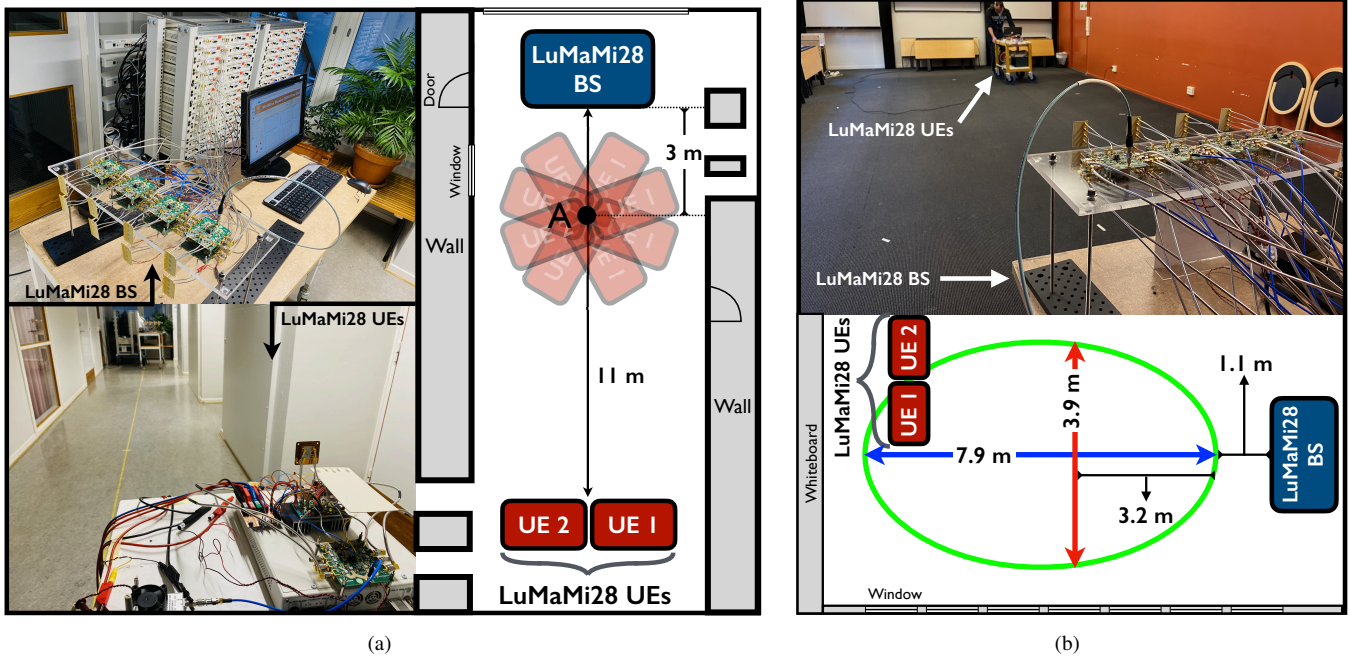


Fig. 9. Photos and indoor maps of measurement campaign in static/mobility environments. There is no obstruction between the LuMaMi28 BS and UEs in all the environments. Both static and mobility measurement places are surrounded by concrete wall and clear windows. (a) setup for the static environment at a long corridor in E-huset building. Spot A is the location for UE rotation test. (b) setup for the mobility environments at a large lecture hall in the same building. There are three routes for its measurement campaigns; circled (green), vertical (blue), and horizontal routes (red).

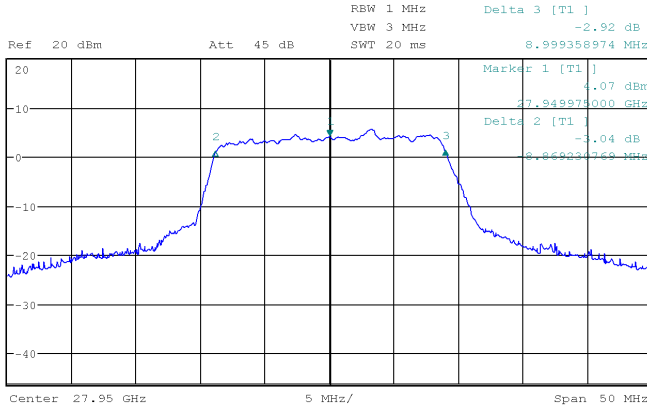


Fig. 10. An UL Tx power spectrum captured at a FEM Tx port. Max hold mode was used for peak detection. In this captured spectrum, the peak power is 4.07 dBm at the center frequency of 27.95 GHz.

present measurement details in the lecture room in Section V-E.

2) *Metrics*: our evaluation uses Rx power for path loss measurement, channel gain for UL channel capturing, and UL throughput and throughput gain for mobility test. The individual throughput of each UE were recorded in real-time. The throughput gain is computed as the ratio of the measured UL throughputs with and without antenna selection.

3) *Antenna Type*: the UE1 was equipped with the yagi antenna (Fig. 8(a)), and the UE2 equipped with the patch antenna (Fig. 8(b)). This configuration is identical over all the measurement campaigns. During the UL throughput measurements, two co-located UEs moved together to provide the same mobility environment to both UEs as possible.

4) *Equalization*: the LuMaMi28 BS performs a fully-digital beamforming. In the measurement campaign, the MRC and ZF

equalizers in (6) were used to decode UL signals from two UEs.

### B. Path Loss Measurement

Prior to the performance measurement, we conducted the Rx power measurement of the LuMaMi28 BS for link-budget calculation. A signal generator (E8257D) was used, as an IF signal generator, to guarantee an accurate power for transmission. The output of E8257D was connected with one FRECON, one FEM, and one antenna in order, i.e., only the SDR part was replaced with E8257D from an UE setup. Both yagi and patch UE antennas were employed for the link-budget calculation. The IF Rx powers of 16 FRECONs in the LuMaMi28 BS were measured by using a spectrum analyzer (FSU50). We selected the following distances (m),  $\mathcal{D}_p = \{3, 5, 7, 9, 11\}$ . At each Tx and Rx locations, the Rx power measurements were conducted with boresight to the center of the LuMaMi28 BS array<sup>5</sup>.

Based on the measured Rx power values, we calculated a measured FSPL for the distance  $d$  between Tx and Rx antennas, and compare with its theoretical number. Effective isotropic radiated power (EIRP) is the hypothetical power radiated by a isotropic Tx antenna in the strongest direction and defined as

$$\text{EIRP}(\text{dBm}) = P_{\text{tx}} + G_{\text{tx}}^c - L_{\text{tx}}^c + G_{\text{tx}}^a \quad (10)$$

where  $P_{\text{tx}}$  is the Tx power (IF input),  $G_{\text{tx}}^c$  the effective Tx gain of FRECON and FEM,  $L_{\text{tx}}^c$  the cable loss in the Tx side, and  $G_{\text{tx}}^a$  the Tx antenna gain. Using the EIRP, the measured FSPL is

$$\text{PL}_m(\text{dB}) = \text{EIRP} - (P_{\text{rx}} - G_{\text{rx}}^c + L_{\text{rx}}^c - G_{\text{rx}}^a) \quad (11)$$

<sup>5</sup>The array antennas of BS and UEs were aligned with co-polarization. The same antenna setup was applied for all experiments.

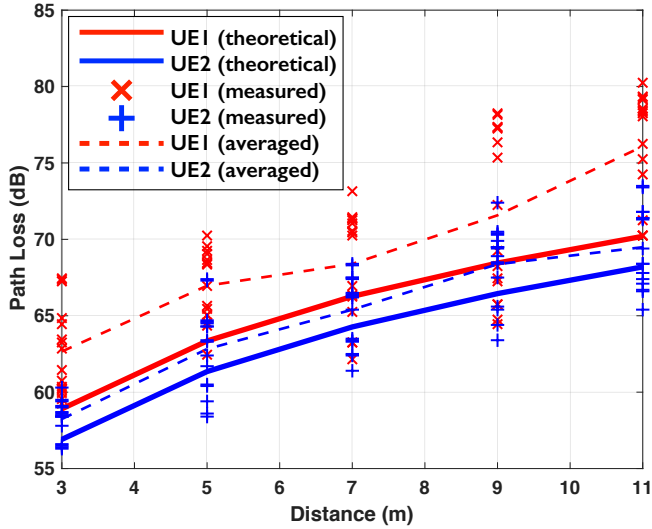


Fig. 11. Measured path loss values of UE1 (yagi)/UE2 (patch) for 27.95 GHz indoor channels. At each distance, the FSPLs measured from 16 FRECON are represented. The dotted red (UE1)/blue (UE2) lines are the averaged values of the measured path loss.

where  $P_{rx}$  is the Rx power (IF output),  $G_{rx}^c$  the effective Rx gain of FRECON,  $L_{rx}^c$  the cable loss in the Rx side, and  $G_{rx}^a$  the Rx antenna gain. The theoretical FSPL is

$$PL_{th}(dB) = 20\log_{10}\left(\frac{4\pi df}{c}\right) - G_{tx}^a - G_{rx}^a \quad (12)$$

where  $f$  is the carrier frequency, and  $c$  is the speed of light. Fig. 11 shows the measured FSPL values of UE1 (yagi)/UE2 (patch) for 27.95 GHz indoor channels, from (10)-(12). Also, the average curves of the measured FSPLs for each UE are shown. It is shown that the both averaged FSPLs are generally quite close to the theoretical ones. The UE1's gap between averaged and theoretical FSPL is relatively larger than that of the UE2. It is conjectured that the yagi antenna beam is relatively more sensitive to placement or angle of departure (AoD) although a boresight measurement was applied for measuring the Rx power at the BS.

### C. UL channel capturing

This subsection studies potential gains achieved by the proposed antenna-selection algorithm. To better assess the potential gain, real-channel capture experiments were conducted where the captured data is the UL channels between LuMaMi28 BS and UEs. This was done by a flexible implementation at the BS side, which allows for capturing the signal from the UL pilots in real-time and then saving the channel to be used for further analysis in the post-processing. Static measurements were done with two UEs at a distance of 3, 7, and 11 m from the BS. UE1 and UE2 have the yagi and patch antenna array, respectively. The UL channels from the two UEs were collected every 10 ms for a total duration of 10 s. For each position, the channels were collected four times, one time for each of the antennas ports in each UE antenna array, such that the potential gain, achieved by switching among the four antenna ports, later could be assessed by comparing the channel gain, i.e., the squared amplitudes of the channel coefficients, for each of the antenna ports.

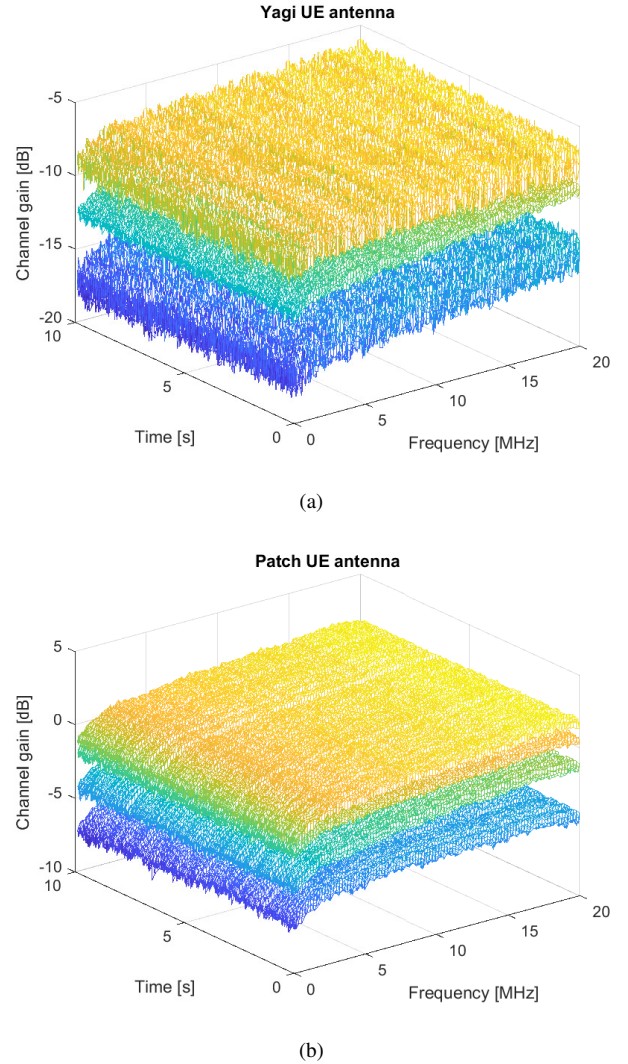


Fig. 12. Channel gain for all four antennas over time and frequency, summed for all BS antennas (a) yagi antenna (b) patch antenna

The channel gain over time and frequency, as summed over the BS RF chains, is shown in Fig. 12(a) for the yagi antenna array and in Fig. 12(b) for the patch antenna array. These captures are at the 3 m distance from the BS and each of the levels corresponds to one antenna port in the array. What can be seen in the figures are that in time the channel response is flat, as expected for a static measurement. In frequency it is close to flat, although slightly decaying for the lower part of the bandwidth. In Fig. 12(a) the channel response varies more between the samples and the total channel gain is lower than what is seen in Fig. 12(b), where the response does not vary as much between the samples. These observations are in line with the fact that the yagi antenna has a wider bandwidth and lower gain, while the patch antenna has a more narrow bandwidth and higher gain. In Fig. 12(a), it can be observed that one antenna port clearly has a higher channel gain than the others. There is also a clear second strongest antenna while the two last ones are overlapping and can hence not be visually separated from this figure. In Fig. 12(b), the channel gain of the four antenna ports are easier to distinguish between. Overall, it can be concluded



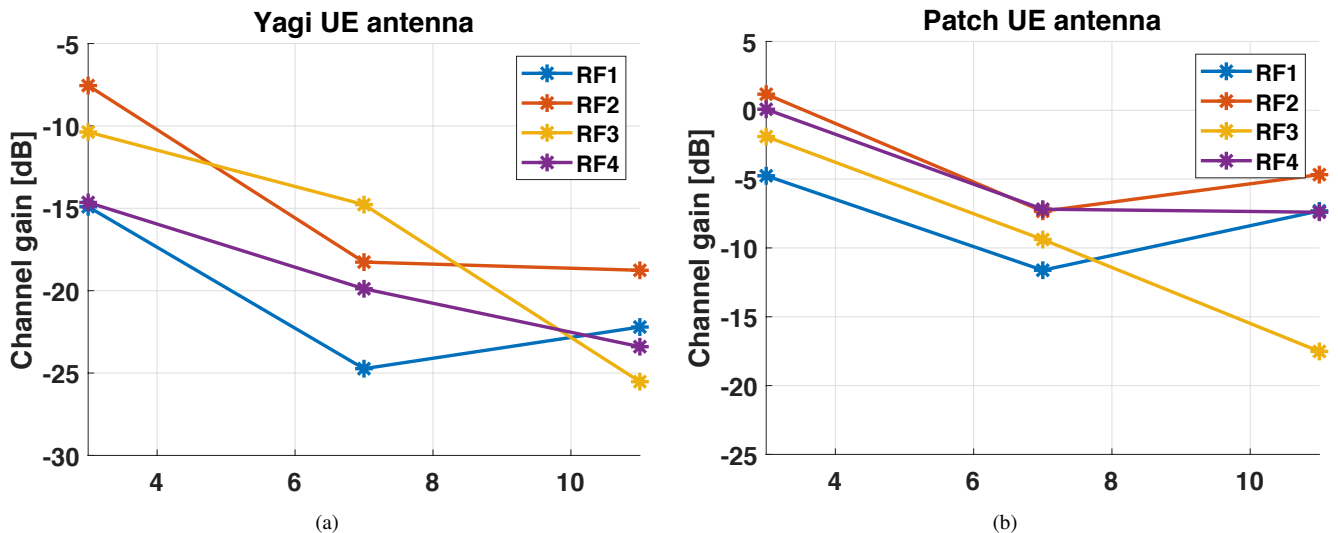


Fig. 13. Channel gain for all four antennas over time and frequency, summed for all BS antennas (a) yagi antenna (b) patch antenna

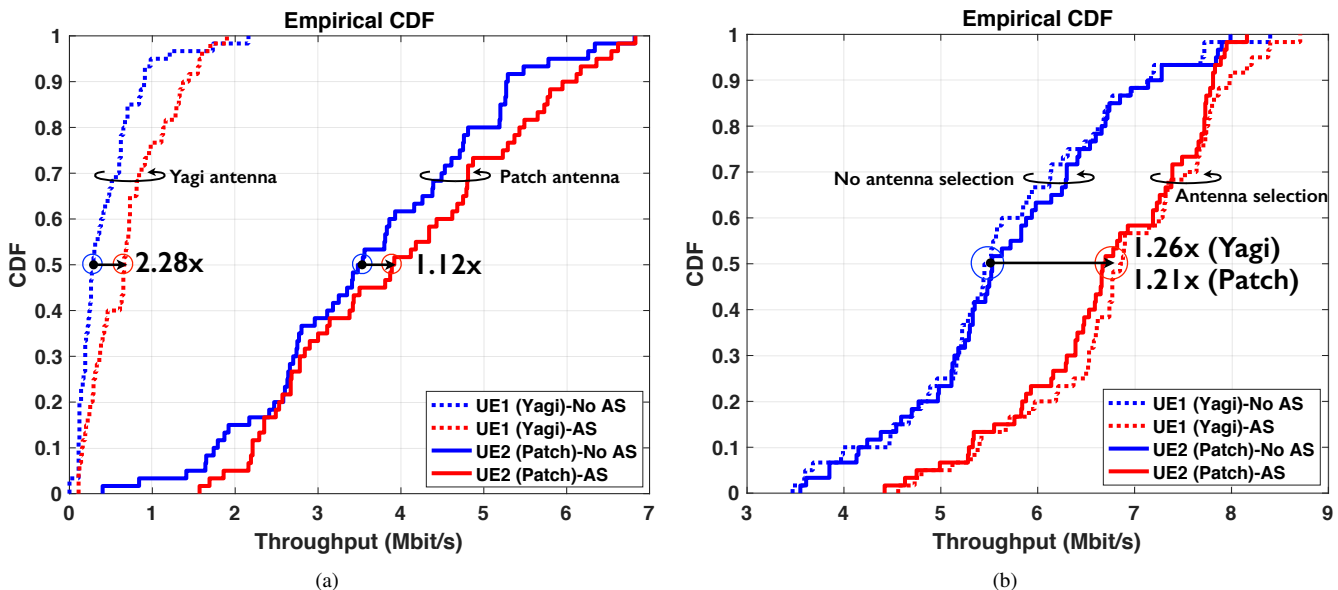


Fig. 14. Throughput CDFs of UEs rotating between  $-90^\circ$  and  $90^\circ$  at a fixed spot. The dotted/solid lines indicate the CDF of the UE1 with yagi antenna and the UE2 with patch antenna, respectively. The red/blue curves are for antenna selection/no antenna selection, respectively. (a) MRC (b) ZF.

that there definitely are differences in terms of channel gain depending on the chosen antenna port and hence, there is indeed a gain to be achieved by switching between them.

To further investigate the gain that can be achieved by switching between the UE antenna ports, the average channel gain at different distances for all the antenna ports can be seen in Fig. 13(a) for the yagi antenna array and in Fig. 13(b) for the patch antenna array. The channel gain here is averaged over time and frequency and summed for all BS RF chains. During the measurements, depending on the distance and UE antenna port measured, parts of the captures were lost. It is probably due to lost synchronization, influenced by weak signal at a moment. These parts were removed from further analysis. It is seen in Fig. 13 that again the higher gain of the patch antenna translates into higher channel gains, compared to the yagi antenna. Looking at each measured position, one can observe that in most cases the channel to one antenna port

is significantly stronger than the other three. However, it is not necessarily the same at another position. Translating this to numbers in terms of achievable gain by using UE-antenna steering, the gains for the yagi antenna at 3, 7, and 11 m are between 2.8 – 7.4, 3.5 – 10.0, and 3.5 – 6.8 dB, respectively. For the patch antenna, the corresponding gains are between 1.1 – 5.9, 0 – 4.4, and 2.6 – 12.8 dB, respectively. It infers that selecting an RF port with the highest channel magnitude can provide a significant benefit for indoor mmWave environment. The following subsections show the actual benefit of antenna-selection, operated in LuMaMi28, in various indoor scenarios.

#### D. UE Rotation Test

We would like to verify an actual throughput gain of LuMaMi28's antenna selection, and study whether it is affected by different UE antennas. We start by the UE rotation test in the static environment described in Fig. 9(a). A fixed spot,

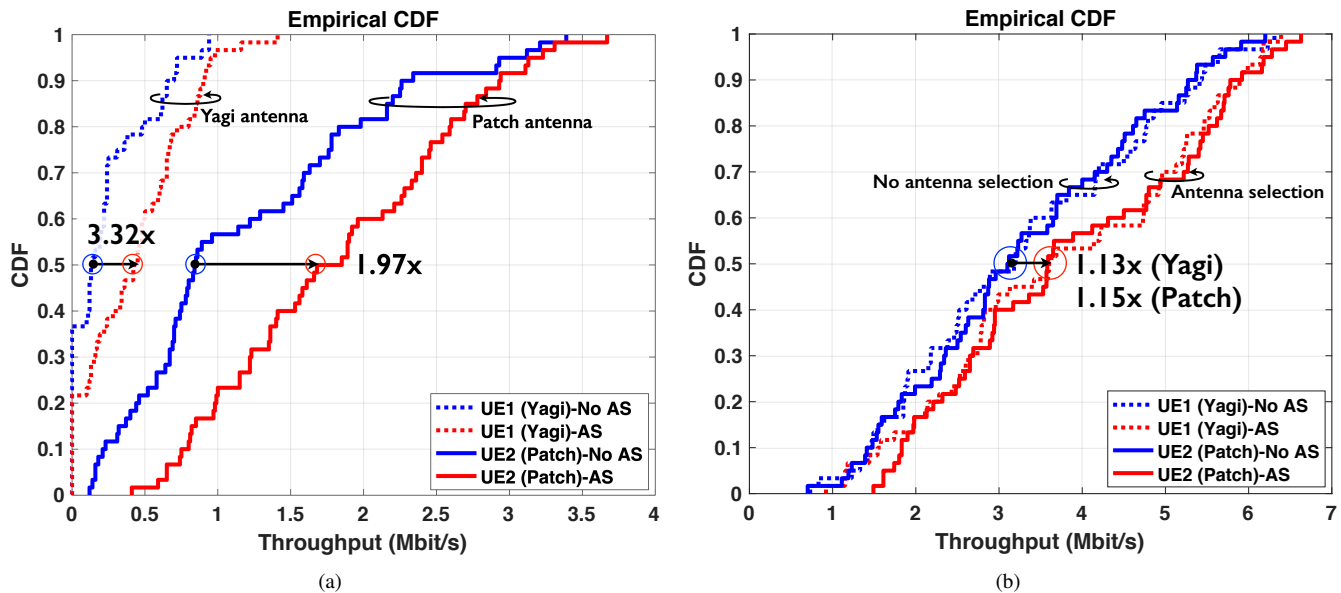


Fig. 15. Throughput CDFs of UEs moving in the horizontal route (around 3 km/h). The dotted/solid lines indicate the CDF of the UE1 with yagi antenna and the UE2 with patch antenna, respectively. The red/blue curves are for antenna selection/no antenna selection, respectively. (a) MRC (b) ZF.

marked as “A” in Fig. 9(a), was selected for the rotation test. The distance between the spot “A” and the LuMaMi28 BS was 3 m. Assuming that the direction to the BS is  $0^\circ$ , two UEs co-located on the moving cart kept rotating between  $-90^\circ$  and  $90^\circ$ , during the measurements. Real-time UL throughputs of each UE were simultaneously recorded while four consecutive experiments were separately performed for with/without antenna selection and different equalizers, i.e., MRC and ZF.

Fig. 14 plots CDFs of the UEs’ UL throughput of LuMaMi28 with/without antenna selection. For MRC equalizer, the median throughput-gain of UE1 through antenna selection is higher than that of UE2, i.e.,  $2.28\times$  for yagi and  $1.12\times$  for patch antenna, as shown in Fig. 14(a). The UE2 UL throughput is, however, higher than that of UE1, both with and without antenna selection. The UE2 has a median throughput of 3.89 and 3.48 Mbit/s while the UE1 only achieves 0.66 and 0.29 Mbit/s, with and without antenna selection, respectively. It can be seen that two UEs’ UL signals interfere with each other, but UE1 is affected by a larger inter-user interference (IUI) from UE2 since UE2 has higher Tx antenna gain. For ZF, the CDF curves of UE1 and UE2 are almost identical as shown in Fig. 14(b). The UE1 obtains a bit higher median throughput-gain than UE2 by using antenna selection, i.e.,  $1.26\times$  for UE1 and  $1.21\times$  for UE2. This result shows that, in case where the IUI is eliminated by the ZF equalizer, a larger beam-width of yagi antenna is useful for antenna selection in the rotating environment at the fixed spot. It translates into higher throughput gain than the use of patch antenna array.

#### E. UE Mobility Test

To evaluate the LuMaMi28’s performance in mobility environments, we considered horizontal, vertical, and circled routes for mobility environments, as seen in Fig. 9(b).

1) *Horizontal Route*: Fig. 15 plots CDFs of the UEs’ UL throughput in the horizontal route. With MRC, the UE1 (yagi) and UE2 (patch) achieve a median throughput-gain of  $3.32\times$

and  $1.12\times$ , respectively, through antenna selection. However, the UE2 has  $4\times$  (antenna selection) and  $6.54\times$  (no antenna selection) higher median-throughput than the UE1. When ZF is applied, the difference between UE1 and UE2 is marginal. The throughput gain through antenna selection is  $1.13\times$  and  $1.15\times$  for the UE1 and UE2, respectively. For both MRC and ZF, a similar tendency is also seen, as compared to the UE rotation test. The reason that the throughputs in this mobility test are generally worse, as compared to those in the rotation test, was affected by larger path loss and mobility environment.

2) *Vertical Route*: Fig. 16 plots CDFs of the UEs’ UL throughput in the vertical route. For MRC, the median throughput-gains of UE1 (yagi) and UE2 (patch), by using antenna selection, are marginal, as shown in Fig. 16(a). It can be seen that antenna selection is generally not very beneficial when moving to the BS direction or its opposite. One interesting observation is that, there is a gap between the peak throughputs of UE1 with/without antenna selection, i.e., 6.4 Mbit/s and 4.43 Mbit/s, respectively, which is a  $1.14\times$  difference. The difference of peak throughput could be related with narrower beam-width but higher gain of patch UE antenna. It could provide a room for antenna selection, as the distance between from the LuMaMi28 BS is close. For ZF, the throughput curves between two UEs are almost same. Also, those between with/without antenna selection have no significant difference. It can be seen because the interference elimination by using ZF dominantly affects each UL throughput improvement. One remarkable thing is that, the antenna selection yields an improvement of lowest throughput of both UEs for ZF, i.e.,  $1.63\times$  (UE1) and  $1.83\times$  (UE2), as shown in Fig. 16(b). It shows that the throughput gain by using antenna selection could be obtained in noise-limited situations, where the performance is not dominated by the ZF equalizer.

3) *Circled Route*: Fig. 17 plots CDFs of the UEs’ UL throughput in the circled route. For MRC, UE2 (patch) obtains a median throughput gain of  $1.66\times$  through antenna selection

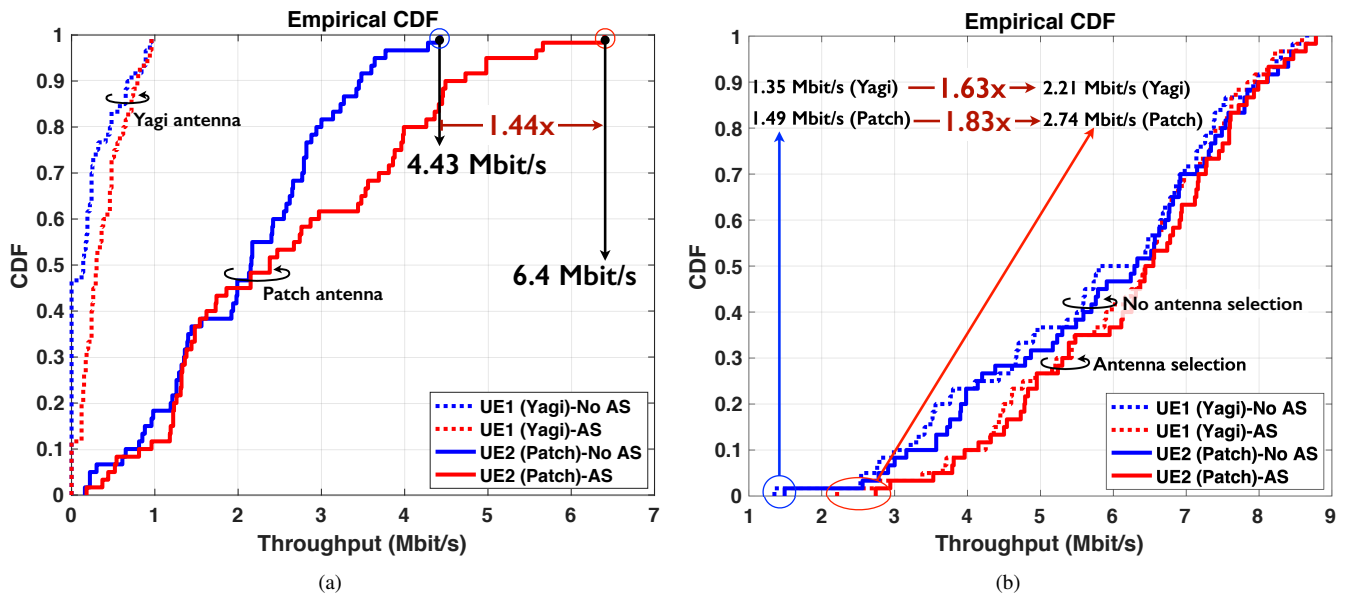


Fig. 16. Throughput CDFs of UEs moving in the vertical route (around 3 km/h). The dotted / solid lines indicate the CDF of the UE1 with yagi antenna and the UE2 with patch antenna, respectively. The red / blue curves are for antenna selection / no antenna selection, respectively. (a) MRC (b) ZF.

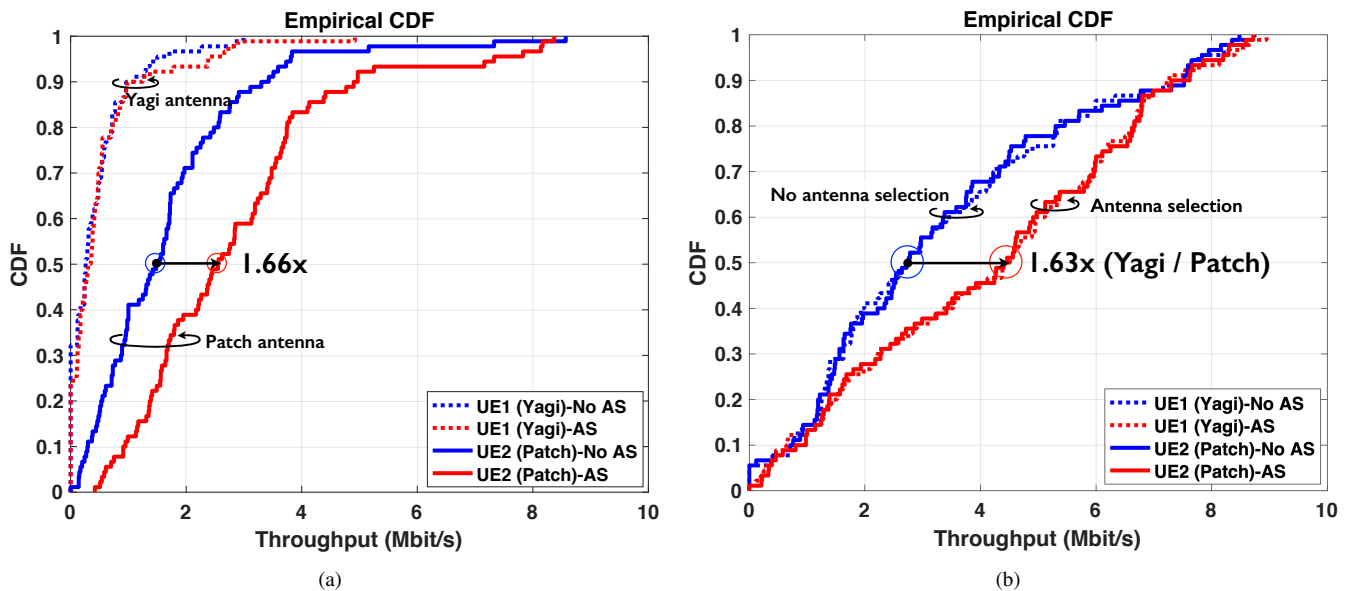


Fig. 17. Throughput CDFs of UEs moving in the circled route (around 3 km/h). The dotted / solid lines indicate the CDF of the UE1 with yagi antenna and the UE2 with patch antenna, respectively. The red / blue curves are for antenna selection / no antenna selection, respectively. (a) MRC (b) ZF.

while that of UE1 (yagi) is relatively marginal. For ZF, as with the previous experiments, there is no significant difference between the throughputs of two UEs. Also, by using the antenna selection, the two UEs achieve the same median throughput-gains ( $1.63\times$ ). In both MRC and ZF, the two UEs' throughput values are placed over the larger range, as compared to the previous experiments.

## VI. CONCLUDING REMARK

In this paper, we have presented LuMaMi28, real-time 28 GHz massive MIMO systems with UE beam steering. Furthermore, real-time measurement results of LuMaMi28 in static and mobility environments have been provided. To explore the

impact of different UE antennas, we adopted two kinds of array antennas: an yagi array antenna with wider angle coverage and a patch array antenna with higher gain. The main findings from our experiments are summarized as follows.

- The result of captured real-channel data shows that the achievable UE-antenna selection gains are 10.0 dB and 12.8 dB for yagi and patch array antennas, respectively, in a distance range of 3 – 11 m between BS and UE.
- The UE-antenna selection of LuMaMi28 delivers a  $3.32\times$  (yagi) /  $1.97\times$  (patch) increase in the median UL throughput in mobility environments, as compared to no antenna selection.
- In case where the MRC equalizer is employed at the BS,

it is found by overall measurements that the throughput of UE, equipped with patch array antenna, is higher than the UE throughput with yagi array antenna, regardless of antenna selection. In case where the ZF equalizer employed at the BS, on the other hand, two UEs' throughputs have a similar tendency, resulting in almost the same throughput gain by using antenna selection.

We believe that these findings will be an important step forward in our understanding of the potential of UE beam steering in mmWave massive MIMO systems. LuMaMi28 has been designed as a flexible testbed because it is implemented by a combination of FPGA-based SDRs and extensible analog modules. The development of larger-scale massive MIMO systems and novel baseband algorithms is an open area for further research with LuMaMi28.

#### ACKNOWLEDGMENT

The authors would like to thank Dr. Carla D. Paola for providing Yagi array prototype for test.

#### REFERENCES

- [1] S. Singh, M. N. Kulkarni, A. Ghosh, and J. G. Andrews, "Tractable model for rate in self-backhauled millimeter wave cellular networks," *IEEE Journal on Selected Areas in Communications*, vol. 33, no. 10, pp. 2196–2211, May 2015.
- [2] A. Ghosh, T. A. Thomas, M. C. Cudak, R. Ratasuk, P. Moorut, F. W. Vook, T. S. Rappaport, G. R. MacCartney, S. Sun, and S. Nie, "Millimeter-wave enhanced local area systems: A high-data-rate approach for future wireless network," *IEEE Journal on Selected Areas in Communications*, vol. 32, no. 6, pp. 1152–1163, Jun. 2014.
- [3] T. S. Rappaport, S. Sun, R. Mayzus, H. Zhao, Y. Azar, K. Wang, G. N. Wong, J. K. Schulz, M. Samimi, and F. Gutierrez, "Millimeter wave mobile communications for 5G cellular: It will work!" *IEEE Access*, vol. 1, pp. 335–349, 2013.
- [4] E. Bjornson, L. Van der Perre, S. Buzzi, and E. G. Larsson, "Massive MIMO in sub-6 GHz and mmWave: Physical, practical, and use-case differences," *IEEE Wireless Communications*, vol. 26, no. 2, pp. 100–108, Jan. 2019.
- [5] M. Chung, L. Liu, O. Edfors, and F. Sheikh, "Phase noise compensation for OFDM systems exploiting coherence bandwidth," *Proc. IEEE Int. Workshop on Sig. Proc. Adv. in Wireless Comm. (SPAWC)*, pp. 1–5, Jul. 2019.
- [6] M. Chung, L. Liu, and O. Edfors, "Phase-noise compensation for OFDM systems exploiting coherence bandwidth: Modeling, algorithms, and analysis," Jul. 2020, [Online] Available: <https://arxiv.org/pdf/2007.09628.pdf>.
- [7] M. Chung, H. Prabhu, F. Sheikh, O. Edfors, and L. Liu, "Low-complexity fully-digital phase noise suppression for millimeter-wave systems," *Proc. IEEE Int. Symp. on Circ. and Sys. (ISCAS)*, pp. 1–5, Oct. 2020.
- [8] T. S. Rappaport, F. Gutierrez, E. Ben-Dor, J. N. Murdock, Y. Qiao, and J. I. Tamir, "Broadband millimeter-wave propagation measurements and models using adaptive-beam antennas for outdoor urban cellular communications," *IEEE Transactions on Antennas and Propagation*, vol. 61, no. 4, pp. 1850–1859, Dec. 2012.
- [9] M. K. Samimi and T. S. Rappaport, "3-D millimeter-wave statistical channel model for 5G wireless system design," *IEEE Transactions on Microwave Theory and Techniques*, vol. 64, no. 7, pp. 2207–2225, Jun. 2016.
- [10] T. S. Rappaport, G. R. MacCartney, S. Sun, H. Yan, and S. Deng, "Small-scale, local area, and transitional millimeter wave propagation for 5G communications," *IEEE Transactions on Antennas and Propagation*, vol. 65, no. 12, pp. 6474–6490, Aug. 2017.
- [11] A. L. Swindlehurst, E. Ayanoglu, P. Heydari, and F. Capolino, "Millimeter-wave massive MIMO: The next wireless revolution?" *IEEE Communications Magazine*, vol. 52, no. 9, pp. 56–62, Sep. 2014.
- [12] O. El Ayach, S. Rajagopal, S. Abu-Surra, Z. Pi, and R. W. Heath, "Spatially sparse precoding in millimeter wave MIMO systems," *IEEE Transactions on Wireless Communications*, vol. 13, no. 3, pp. 1499–1513, Jan. 2014.
- [13] D. Choudhury, "5G wireless and millimeter wave technology evolution: An overview," *Proc. IEEE MTT-S International Microwave Symposium (IMS)*, pp. 1–4, May 2015.
- [14] A. F. Molisch, V. V. Ratnam, S. Han, Z. Li, S. L. H. Nguyen, L. Li, and K. Haneda, "Hybrid beamforming for massive MIMO: A survey," *IEEE Communications Magazine*, vol. 55, no. 9, pp. 134–141, May 2017.
- [15] J. Brady, N. Behdad, and A. M. Sayeed, "Beamspace MIMO for millimeter-wave communications: System architecture, modeling, analysis, and measurements," *IEEE Transactions on Antennas and Propagation*, vol. 61, no. 7, pp. 3814–3827, Mar. 2013.
- [16] A. Alkhateeb, J. Mo, N. Gonzalez-Prelcic, and R. W. Heath, "MIMO precoding and combining solutions for millimeter-wave systems," *IEEE Communications Magazine*, vol. 52, no. 12, pp. 122–131, Dec. 2013.
- [17] P. V. Amadori and C. Masouros, "Low RF-complexity millimeter-wave beamspace-MIMO systems by beam selection," *IEEE Transactions on Communications*, vol. 63, no. 6, pp. 2212–2223, Dec. 2015.
- [18] V. Venkateswaran, F. Pivitt, and L. Guan, "Hybrid RF and digital beamformer for cellular networks: Algorithms, microwave architectures, and measurements," *IEEE Transactions on Microwave Theory and Techniques*, vol. 64, no. 7, pp. 2226–2243, Jun. 2016.
- [19] F. Sohrabi and W. Yu, "Hybrid analog and digital beamforming for mmWave OFDM large-scale antenna arrays," *IEEE Journal on Selected Areas in Communications*, vol. 35, no. 7, pp. 1432–1443, Apr. 2017.
- [20] R. Vilar, R. Czarny, M. L. Lee, B. Loiseaux, M. Sypek, M. Makowski, C. Martel, T. Crepin, F. Boust, R. Joseph, K. Herberich, T. Bertuch, and J. Marti, "Q-band millimeter-wave antennas: An enabling technology for multigigabit wireless backhaul," *IEEE Microwave Magazine*, vol. 15, no. 4, pp. 121–130, May 2014.
- [21] T. Kwon, Y. G. Lim, B. W. Min, and C. B. Chae, "RF lens-embedded massive MIMO systems: Fabrication issues and codebook design," *IEEE Transactions on Microwave Theory and Techniques*, vol. 64, no. 7, pp. 2256–2271, Jul. 2016.
- [22] W. Hong, K. Baek, and S. Ko, "Millimeter-wave 5G antennas for smartphones: Overview and experimental demonstration," *IEEE Transactions on Antennas and Propagation*, vol. 65, no. 12, pp. 6250–6261, Aug. 2017.
- [23] S. Shinjo, K. Nakatani, K. Tsutsumi, and H. Nakamizo, "Integrating the front end: A highly integrated RF front end for high-SHF wide-band massive MIMO in 5G," *IEEE Microwave Magazine*, vol. 18, no. 5, pp. 31–40, Jun. 2017.
- [24] K. K. Samanta and C. Clifton, "5G PA implementation and integration aspects," presented at the Workshop (WMJ-3) on PAs for 5G Mobile Communication: Technologies and Challenges, *IEEE International Microwave Symposium (IMS2017)*, Jul. 2017.
- [25] —, "5G challenges and potential PA architectural solutions," presented at the Workshop (WW-03) on Recent Advancements in Wide-Band and Efficient GaN Power Amplifiers, *European Microwave Week (EuMW2017)*, Oct. 2017.
- [26] A. Alkhateeb, O. El Ayach, G. Leus, and R. W. Heath, "Channel estimation and hybrid precoding for millimeter wave cellular systems," *IEEE Journal of Selected Topics in Signal Processing*, vol. 8, no. 5, pp. 831–846, Jul. 2014.

- [27] E. Vlachos, G. C. Alexandropoulos, and J. Thompson, "Wideband MIMO channel estimation for hybrid beamforming millimeter wave systems via random spatial sampling," *IEEE Journal of Selected Topics in Signal Processing*, vol. 13, no. 5, pp. 1136–1150, Aug. 2019.
- [28] X. Gao, L. Dai, S. Han, C. I, and R. W. Heath, "Energy-efficient hybrid analog and digital precoding for MmWave MIMO systems with large antenna arrays," *IEEE Journal on Selected Areas in Communications*, vol. 34, no. 4, pp. 998–1009, Mar. 2016.
- [29] W. Roh, J. Y. Seol, J. Park, B. Lee, J. Lee, Y. Kim, J. Cho, K. Cheun, and F. Aryanfar, "Millimeter-wave beamforming as an enabling technology for 5G cellular communications: Theoretical feasibility and prototype results," *IEEE Communications Magazine*, vol. 52, no. 2, pp. 106–113, Feb. 2014.
- [30] V. Raghavan, A. Partyka, A. Sampath, S. Subramanian, O. H. Koymen, K. Ravid, J. Cezanne, K. Mukkavilli, and J. Li, "Millimeter-wave MIMO prototype: Measurements and experimental results," *IEEE Communications Magazine*, vol. 56, no. 1, pp. 202–209, Jan. 2018.
- [31] B. Yang, Z. Yu, J. Lan, R. Zhang, J. Zhou, and W. Hong, "Digital beamforming-based massive MIMO transceiver for 5G millimeter-wave communications," *IEEE Transactions on Microwave Theory and Techniques*, vol. 66, no. 7, pp. 3403–3418, May 2018.
- [32] L. Kuai, J. Chen, Z. H. Jiang, C. Yu, C. Guo, Y. Yu, H. Zhou, and W. Hong, "A N260 band 64 channel millimeter wave full-digital multi-beam array for 5G massive MIMO applications," *IEEE Access*, vol. 8, no. 7, pp. 47 640–47 653, May 2020.
- [33] M. Chung, L. Liu, O. Edfors, and F. Tufvesson, "Demo: Millimeter-wave massive MIMO testbed with hybrid beamforming," *Proc. IEEE Wireless Comm. and Net. Conf. Workshops (WCNCW)*, pp. 1–2, Apr. 2020.
- [34] M. Chung, L. Liu, A. Johansson, M. Nilsson, O. Zander, Z. Ying, F. Tufvesson, and O. Edfors, "Millimeter-wave massive MIMO testbed with hybrid beamforming," *Proc. Asilomar Conference on Signals, Systems, and Computers*, pp. 1–5, Nov. 2020.
- [35] S. Malkowsky, J. Vieira, L. Liu, P. Harris, K. Nieman, N. Kundargi, I. Wong, F. Tufvesson, V. Öwall, and O. Edfors, "The world first real-time testbed for massive MIMO: Design, implementation, and validation," *IEEE Access*, vol. 5, pp. 9073–9088, 2017.
- [36] J. Vieira, F. Rusek, O. Edfors, S. Malkowsky, L. Liu, and F. Tufvesson, "Reciprocity calibration for massive MIMO: Proposal, modeling, and validation," *IEEE Transactions on Wireless Communications*, vol. 16, no. 5, pp. 3042–3056, 2017.
- [37] C. B. Peel, B. M. Hochwald, and A. L. Swindlehurst, "A vector-perturbation technique for near-capacity multiantenna multiuser communication-part I: channel inversion and regularization," *IEEE Transactions on Communications*, vol. 53, no. 1, pp. 195–202, 2005.
- [38] S. Hur, T. Kim, D. J. Love, J. V. Krogmeier, T. A. Thomas, and A. Ghosh, "Millimeter wave beamforming for wireless backhaul and access in small cell networks," *IEEE Transactions on Communications*, vol. 61, no. 10, pp. 4391–4403, Oct. 2013.
- [39] S. Sesia, I. Toufik, and M. Baker, *LTE: the UMTS long term evolution*. New York: John Wiley & Sons, 2009.
- [40] C. Di Paola, S. Zhang, K. Zhao, Z. Ying, T. Bolin, and G. F. Pedersen, "Wideband beam-switchable 28 GHz quasi-yagi array for mobile devices," *IEEE Transactions on Antennas and Propagation*, vol. 67, no. 11, pp. 6870–6882, Jul. 2019.